Ultrafast Three-Dimensional Imaging of Lattice Dynamics in Individual Gold Nanocrystals

J. N. Clark *et al.*

Science **341**, 56 (2013);
DOI: 10.1126/science.1236034

Science (print ISSN 0036-8075; online ISSN 1095-9203) is published weekly, except the last week in December, by the American Association for the Advancement of Science, 1200 New York Avenue NW, Washington, DC 20005.

no known gamma-ray burst (GRB) with a coincident position on a time scale commensurate with previous tentative detections of short-duration radio emission (*6*). GRBs have highly beamed gamma-ray emission (*21*), and, if FRBs are associated with them, the radio emission must be beamed differently. By using the distances in Table 1, we found that the comoving volume contains ~10^9 late-type galaxies (*22*), and the FRB rate is therefore $R_{FRB} \sim 10^{-3}$ year^{-1} per galaxy. R_{FRB} is thus inconsistent with $R_{GRB} \sim 10^{-6}$ year^{-1} per galaxy, even when beaming of emission is accounted for (*21*). Soft gamma-ray repeaters (SGRs) undergo giant bursts at a rate consistent with FRBs (*23*), and the energy within our band is well within the budget of the few known SGR giant burst cases (*24*).

Another postulated source class is the interaction of the magnetic fields of two coalescing neutron stars (*25*). However, the large implied FRB luminosities indicate that coalescing neutron stars may not be responsible for FRBs. Furthermore, R_{FRB} is substantially higher than the predicted rate for neutron star mergers. Black hole evaporation has also been postulated as a source of FRBs; however, the predicted luminosity within our observing band far exceeds the energy budget of an evaporation event (*26*).

The core-collapse supernova (ccSN) rate of $R_{ccSN} \sim 10^{-2}$ year^{-1} per galaxy (*27*) is consistent with R_{FRB}. There is no known mechanism to generate an FRB from a lone ccSN. It may, however, be possible that a ccSN with an orbiting neutron star can produce millisecond-duration radio bursts during the interaction of the ccSN explosion and the magnetic field of the neutron star (*28*), although the need for an orbiting neutron star will make these rarer.

As extragalactic sources, FRBs represent a probe of the ionized IGM. Real-time detections and immediate follow-up at other wavelengths may identify a host galaxy with an independent redshift measurement, thus enabling the IGM baryon content to be determined (*12*). Even without host identifications, further bright FRB detections will be a unique probe of the magneto-ionic properties of the IGM.

References and Notes

1. M. J. Keith *et al.*, *Mon. Not. R. Astron. Soc.* **409**, 619–627 (2010).
2. Materials and methods are available as supplementary materials on *Science* Online.
3. J. M. Cordes, *SKA Memo Ser.* **97**, 1 (2009).
4. D. R. Lorimer *et al.*, *Science* **318**, 777–780 (2007); 10.1126/science.1147532.
5. E. F. Keane, B. W. Stappers, M. Kramer, A. G. Lyne, *Mon. Not. R. Astron. Soc.* **425**, L71–L75 (2012).
6. K. W. Bannister, T. Murphy, B. M. Gaensler, J. E. Reynolds, *Astrophys. J.* **757**, 38 (2012).
7. E. Rubio-Herrera, B. W. Stappers, J. W. T. Hessels, R. Braun, *Mon. Not. R. Astron. Soc.* **428**, 2857–2873 (2013).
8. S. Burke-Spolaor *et al.*, *Astrophys. J.* **727**, 18 (2011).
9. The Lorimer burst is designated as FRB 010724; this date is a correction to that in the original paper.
10. J. M. Cordes, T. J. W. Lazio (2002), http://arxiv.org/abs/astroph/0207156.
11. J. S. Deneva, J. M. Cordes, T. J. W. Lazio, *Astrophys. J.* **702**, L177–L181 (2009).
12. K. Ioka, *Astrophys. J.* **598**, L79–L82 (2003).
13. S. Inoue, *Mon. Not. R. Astron. Soc.* **348**, 999–1008 (2004).
14. I. P. Williamson, *Mon. Not. R. Astron. Soc.* **157**, 55 (1972).
15. N. D. R. Bhat *et al.*, *Astrophys. J.* **605**, 759–783 (2004).
16. R. C. Roeder, R. T. Verreault, *Astrophys. J.* **155**, 1047 (1969).
17. H. Isliker, A. O. Benz, *Astron. Astrophys. Suppl. Ser.* **104**, 145 (1994).
18. R. N. Manchester *et al.*, *Mon. Not. R. Astron. Soc.* **328**, 17–35 (2001).
19. M. Bagchi, A. C. Nieves, M. McLaughlin, *Mon. Not. R. Astron. Soc.* **425**, 2501–2506 (2012).
20. S. Burke-Spolaor *et al.*, *Mon. Not. R. Astron. Soc.* **416**, 2465–2476 (2011).
21. D. A. Frail *et al.*, *Astrophys. J.* **562**, L55–L58 (2001).
22. D. S. Madgwick *et al.*, *Mon. Not. R. Astron. Soc.* **333**, 133–144 (2002).
23. E. O. Ofek, *Astrophys. J.* **659**, 339–346 (2007).
24. K. Hurley *et al.*, *Nature* **434**, 1098–1103 (2005).
25. B. M. S. Hansen, M. Lyutikov, *Mon. Not. R. Astron. Soc.* **322**, 695–701 (2001).
26. M. J. Rees, *Nature* **266**, 333–334 (1977).
27. R. Diehl *et al.*, *Nature* **439**, 45–47 (2006).
28. A. E. Egorov, K. A. Postnov, *Astron. Lett.* **35**, 241–246 (2009).
29. N. Spergel *et al.*, *Astrophys. J. Suppl. Ser.* **148**, 175–194 (2003).

Acknowledgments: This research has made use of the NASA/IPAC (Infrared Processing and Analysis Center) Extragalactic Database (NED), which is operated by the Jet Propulsion Laboratory, California Institute of Technology, under contract with NASA. This research has made use of data obtained from the High Energy Astrophysics Science Archive Research Center, provided by NASA's Goddard Space Flight Center. Part of this research was carried out at the Jet Propulsion Laboratory, California Institute of Technology, under a contract with NASA. The Parkes radio telescope is part of the Australia Telescope National Facility, which is funded by the Commonwealth of Australia for operation as a National Facility managed by CSIRO. Part of this research was conducted because of the support of CAASTRO through project number CE110001020. D.T. gratefully acknowledges the support of the Science and Technology Facilities Council and CSIRO Astronomy and Space Science in his Ph.D. studentship. N.D.R.B. is supported by a Curtin Research Fellowship (CRF12228).

Supplementary Materials

www.sciencemag.org/cgi/content/full/341/6141/53/DC1
Materials and Methods
Figs. S1 to S4
Table S1
References (*30*, *31*)

19 February 2013; accepted 30 May 2013
10.1126/science.1236789

Ultrafast Three-Dimensional Imaging of Lattice Dynamics in Individual Gold Nanocrystals

J. N. Clark,[1]* L. Beitra,[1] G. Xiong,[1] A. Higginbotham,[2] D. M. Fritz,[3] H. T. Lemke,[3] D. Zhu,[3] M. Chollet,[3] G. J. Williams,[3] M. Messerschmidt,[3] B. Abbey,[4] R. J. Harder,[5] A. M. Korsunsky,[6,7] J. S. Wark,[2] I. K. Robinson[1,7]

Key insights into the behavior of materials can be gained by observing their structure as they undergo lattice distortion. Laser pulses on the femtosecond time scale can be used to induce disorder in a "pump-probe" experiment with the ensuing transients being probed stroboscopically with femtosecond pulses of visible light, x-rays, or electrons. Here we report three-dimensional imaging of the generation and subsequent evolution of coherent acoustic phonons on the picosecond time scale within a single gold nanocrystal by means of an x-ray free-electron laser, providing insights into the physics of this phenomenon. Our results allow comparison and confirmation of predictive models based on continuum elasticity theory and molecular dynamics simulations.

Coherent lattice vibrations (phonons) in solids play an important role in many phenomena such as melting (*1*–*5*), phase transitions (*6*), bond softening (*7*) and hardening (*8*), and ferroelectricity (*9*). Ultrashort (femtosecond) laser pulses have been used to reveal great detail about the dynamics of these phenomena; however, many of these studies have been confined to bulk samples or ensembles of nanoparticles. With nanoparticles playing an increasingly important role in technology, from catalysis (*10*) and photonic devices (*11*) to single-particle mass spectrometry (*12*) and sensing, understanding the mechanical and dynamical properties of single nanoparticles becomes very important as many of the processes occur on femtosecond (fs) and picosecond (ps) time scales.

The characterization of lattice displacements in individual nanoparticles over very short time scales with atomic sensitivity has been challenging. The interrogation of individual particles is important, as ensemble heterogeneity can give the

[1]London Centre for Nanotechnology, University College London, London WC1E 6BT, UK. [2]Department of Physics, Clarendon Laboratory, University of Oxford, Parks Road, Oxford OX1 3PU, UK. [3]Linac Coherent Light Source, SLAC National Accelerator Laboratory, 2575 Sand Hill Road, Menlo Park, CA 94025, USA. [4]ARC Centre of Excellence for Coherent X-ray Science, Department of Physics, La Trobe University, Bundoora, Victoria 3086, Australia. [5]Advanced Photon Source, Argonne, IL 60439, USA. [6]Department of Engineering Science, University of Oxford, Parks Road, Oxford OX1 3PJ, UK. [7]Research Complex at Harwell, Didcot, Oxfordshire OX11 0DE, UK.

*Corresponding author. E-mail: jesse.clark@ucl.ac.uk

impression of considerably shorter-lived dynamics than actually exist (*13*, *14*) and may hide the presence of high-order phonon modes or anharmonicity. Optical pump-probe experiments have shown promising results, particularly for single particles (*15*) over very short time scales; however, because of the long wavelength of the probe, atomic-scale motions cannot be measured without relying on interpretations from continuum elasticity theory. Pump-probe experiments on nanoparticles using electrons or x-rays overcome this problem by probing the atomic-scale motions directly (*16*, *17*). The low scattering cross sections of x-rays and the (relatively) low number of photons in the ultrashort x-ray pulses from plasma sources (required for the short pulse duration) limit the ability to study individual nanoparticles. Likewise, for electrons, the small number of electrons per ultrashort pulse has meant that probing individual nanoparticles has been difficult. The increased flux of synchrotron sources in comparison to plasma sources provides a sufficient number of x-ray photons to probe individual nanoparticles, but at the expense of time resolution. This provides a strong motivation to develop ultrafast pump-probe x-ray diffraction methods on individual nanocrystals using x-ray free-electron lasers (XFELs) (*18*). Using this approach, one can elucidate the elastic response of the atomic lattice to laser irradiation while simultaneously obtaining high-resolution real-space images of the deformation field inside the nanocrystal by means of Bragg coherent diffraction imaging (BCDI) (*19*, *20*).

BCDI is sensitive to very small variations in strain within nanocrystals as it recovers the projected distortion of the electron density with picometer (pm) sensitivity. The recovered image comprises the amplitude, which is related to the electron density, and the phase, $\phi(\boldsymbol{r})$, which is related to the (vector) displacement field $\boldsymbol{u}(\boldsymbol{r})$ of the atoms from the ideal lattice points and the scattering vector $\boldsymbol{Q}$ via $\phi(\boldsymbol{r}) = \boldsymbol{u}(\boldsymbol{r})\cdot\boldsymbol{Q}$ (*21*). Images obtained from noncoplanar Bragg peaks can be combined to recover the full displacement field (*22*).

Figure 1 shows a schematic of the experimental arrangement for ultrafast BCDI, which was performed at the x-ray pump probe (XPP) instrument at the Linac Coherent Light Source (LCLS). Truncated octahedra gold nanocrystals, ~300 to 400 nm in diameter (*21*), were placed at the center of a diffractometer. A Ti-sapphire laser with a wavelength of 800 nm and a pulse length of 50 fs [full duration at half-maximum (FDHM)] was used to generate coherent acoustic phonons in the gold nanocrystals. The incident fluence used in the experiment was 1 mJ/cm^2. The sample was illuminated with 80-fs (FDHM), 9.2-keV x-rays generated by LCLS operating at a repetition rate of 120 Hz. A Si (111) monochromator was used to select ~1 eV bandwidth. Beryllium lenses were used to focus the illumination to an ~30 μm by 30 μm spot. Multiple nanocrystals were illuminated simultaneously, but orientation differences between them allowed Bragg peaks from individual nanocrystals to be spatially separated on the detector. The relative timing (accurate to sub-ps) of the optical and x-ray pulse was adjusted to provide the time-resolved data with the two beams almost parallel for spatial coincidence. Both fluences were below the damage threshold to allow repeated measurements. The coherent diffraction patterns were recorded with a Cornell-SLAC pixel array detector (CS-PAD) (*23*) positioned 1.2 m from the sample at the gold (111) Bragg peak, a sufficient distance to oversample (*19*) the diffraction patterns. A helium-filled bag was placed between the sample and detector to reduce absorption and scattering from air.

The coherent diffraction patterns that were recorded from an individual nanocrystal (Fig. 2, A and B) show the modulated diffraction fringes, a consequence of the coherent illumination and finite nanocrystal size, which was much smaller than the x-ray beam. The fringes are most prominent in the facetted directions of the nanocrystal. The diffraction pattern collected immediately before the pump laser (Fig. 2A) shows a relatively symmetric fringe pattern, whereas the diffraction pattern collected +60 ps after (Fig. 2B) is more asymmetric, which is attributed to inhomogeneous lattice distortions i.e., an elastic strain gradient. Homogeneous contraction and expansion of the lattice (radial breathing modes) are manifested as a shift of the entire diffraction pattern (*21*) as the average lattice spacing changes across the nanocrystal. Shown in Fig. 2, C and D, is the angular shift of the gold (111) Bragg peak for two nanocrystals, I and II. For each time delay, the center of mass from the sum of 100 diffracted LCLS pulses was used to obtain the angular shift, with the error for each delay point given by the standard deviation. At the center of the rocking curve, ~10^4 diffracted photons are recorded per pulse. The homogeneous lattice expansion and contraction are evident as harmonic motion of the Bragg peak angular shift. Immediately after the arrival of the optical pump laser (positive delay times), the diffraction pattern starts shifting to lower angles. Because the crystal is much bigger than the electromagnetic "skin depth," this behavior is only consistent with an electron-mediated model, such as the "two-temperature" model (*24*) of heating in which electrons are excited first and subsequently transfer energy to the lattice through electron-phonon coupling. The peak shift, $S(\tau)$ as a function of delay time, τ, is fitted by

$$S(\tau) = \sum_{n=1}^{N} A_n \exp\left[-\frac{\tau}{\tau_{d,n}}\right] \times \cos\left[\frac{2\pi}{T_n}(\tau + \tau_{0,n})\right] + C_n \qquad (1)$$

where n is the mode number, N(=2) is the total number of fitted modes, A is the amplitude, τ_d is the decay time, T is the period of the oscillation, and τ_0 is the time offset. Two oscillation modes (red solid curve) are sufficient to fit the data shown in Fig. 2, C and D, within their errors with the fitted parameters summarized in table S1. The fitted values of the two periods from the data for nanocrystal I were 101 and 241 ps, and for nanocrystal II were 90 and 256 ps; the different oscillation periods between nanocrystals were a consequence of unequal sizes. These two oscillation modes are well reproduced by a molecular dynamics (MD) simulation (*21*) (fig. S1). Using the thermal expansion coefficient for bulk gold of 14.4(2) × 10^{-6} K^{-1} and the maximum change in the lattice constant, we estimated the

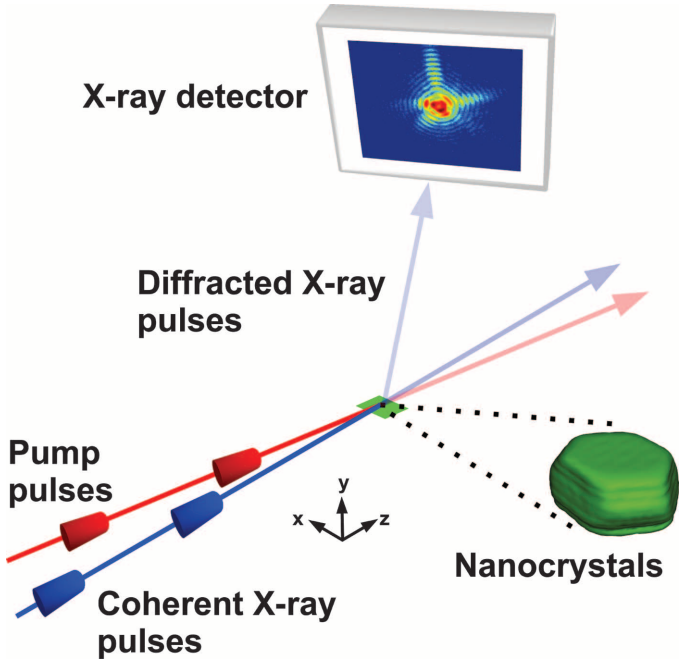

Fig. 1. Ultrafast time-resolved Bragg coherent diffraction imaging. Optical pulses (red) perturb the sample (green), generating phonons. Coherent x-ray pulses (generated from an XFEL) (blue) arrive a short time later. The diffracted pulses are recorded by an area detector, such as a CS-PAD.

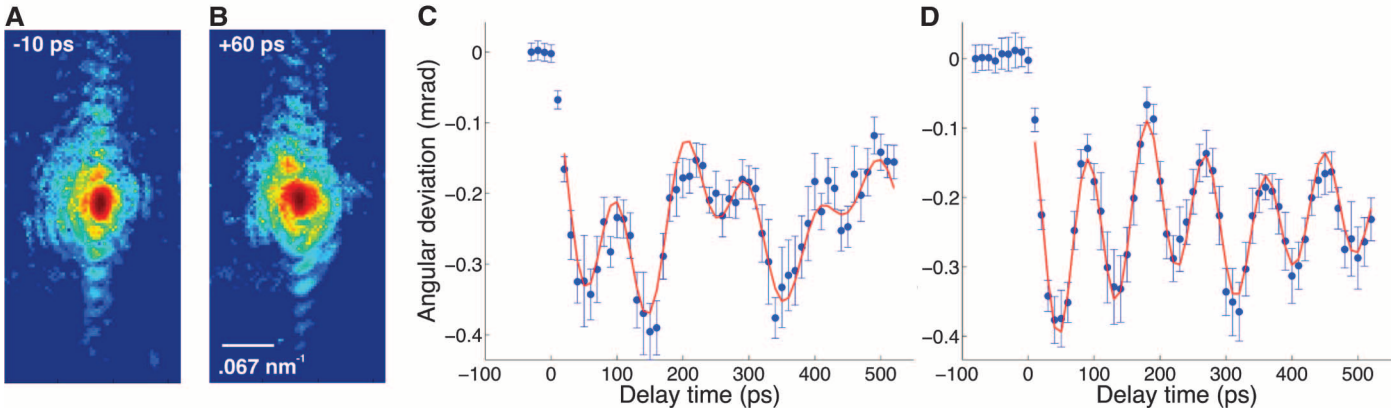

Fig. 2. Time-resolved Bragg coherent diffraction data from single nanocrystals. (**A** and **B**) Experimentally recorded coherent diffraction patterns from a single nanocrystal for delay times of −10 and +60 ps, respectively. The diffraction patterns are the sum of 100 shots and are scaled logarithmically. (**C** and **D**) Gold (111) Bragg peak angular shift as a function of delay time from the same nanocrystal [(C), nanocrystal I] and a different nanocrystal [(D), nanocrystal II]. The blue dots are the experimental data and the solid red line is the modeled peak shift.

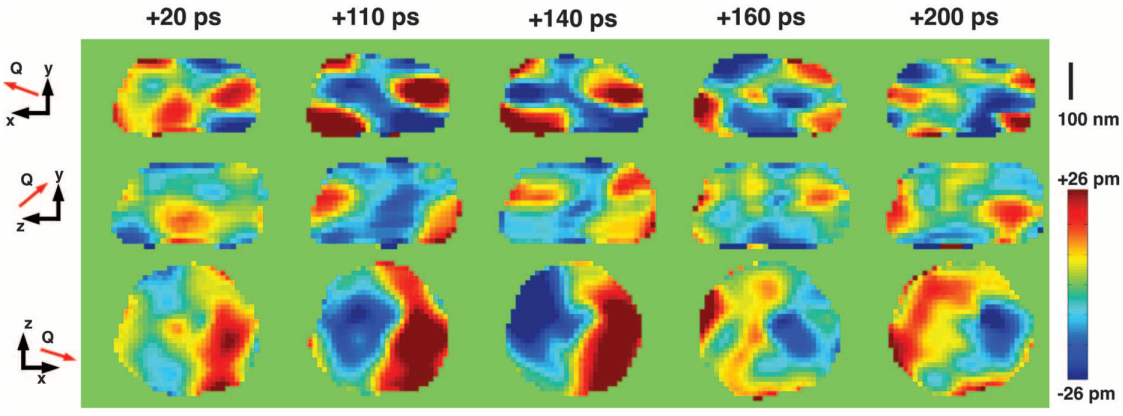

Fig. 3. Imaging of acoustic phonons in a nanocrystal. Orthogonal cut planes through the center of nanocrystal I showing the projected displacement as a function of delay time. Three different viewing directions are shown. The direction of the displacement field is given by the ***Q*** vector in red. For clarity, the range of displacement has been truncated to ±26 pm instead of the full range of ±53 pm.

temperature increase on each pump-probe cycle to be 44 K for each of the two nanocrystals. The fitted vibration amplitudes correspond to a maximum displacement of 600 pm at the surface of the crystal.

The peak position versus delay time shown in Fig. 2 agrees well with previous studies of gold nanoparticles (*13*, *25*, *26*) or thin films (*5*). The important distinction in this study is that we can monitor the behavior of individual nanocrystals using x-ray diffraction rather than the behavior of an ensemble (*13*, *25*, *26*). X-rays provide the structural sensitivity evident in Fig. 2, C and D, where both in-plane and out-of-plane cylinder oscillations are observed owing to the coupling of the ***Q*** vector to both these directions. Notably, the lifetime of the oscillations is relatively long in comparison to previous studies, because there is no ensemble averaging of heterogeneous periods in our experiment (*13*–*15*, *21*).

Thus far, we have identified two clear vibration modes in the expansion of the crystal. Further modes, such as shear modes, can be identified only by imaging the crystal distortions directly because these do not result in a shift of the Bragg peak position. Three-dimensional (3D) images as a function of delay time were obtained for nanocrystal I by collecting 3D coherent diffraction patterns and then recovering the lost phase of the diffracted wavefield by using iterative phase retrieval (*21*, *27*). Complete knowledge of the diffracted wavefield (both amplitude and phase) allows an image of the nanocrystal to be obtained by an inverse Fourier transform. To obtain the missing phase of the diffracted wavefield, an iterative procedure is used that enforces the a priori knowledge that the nanocrystal is isolated, as well as consistency with the measured amplitude of the diffracted wavefield (from the measured intensity). These two constraints are enforced successively until a self-consistent solution is reached.

Figure 3 shows images of the phase of nanocrystal I, displayed as orthogonal cuts through the center for selected times. This phase is the change in the displacement of the crystal, projected onto the diffraction vector ***Q***, whose direction is also shown in Fig. 3. The homogeneous (linear) lattice expansion and contraction resulting from the breathing modes of the nanocrystal have been removed (*21*), leaving only the inhomogeneous component that would manifest itself as a broadening or distortion of the Bragg peak rather than a peak shift. To emphasize the changes, we have subtracted the image at –40 ps from the subsequent times, which removes the contribution of small, static residual stresses in the nanocrystal. The spatial pattern of oscillating regions of expansion and contraction are well within the resolution of the image (*21*), estimated as 51 ± 7, 22 ± 3, and 55 ± 6 nm in the *x*, *y*, and z directions, respectively.

What is particularly evident in Fig. 3 is that the regions of expansion become regions of contraction and vice versa as the delay time increases (movie S1). This spatial and temporal reversal of expansion and contraction is indicative of the presence of a shear vibration mode of higher order than a simple breathing mode. Figure 4 shows the location of selected slices (top row) used to compare the experimental images (middle row) with the theoretical (1, 1) mode of a cylinder (bottom row) with a radius of 200 nm and a height of 220 nm (*21*). The good agreement between the data, theory, and MD simulation (fig. S2) strongly supports the presence of this otherwise invisible higher-order mode. Our observation of this 50-pm amplitude mode in the presence of a 600-pm breathing mode shows the considerable sensitivity gain by BCDI imaging.

The combination of intense, coherent, and ultrashort x-ray pulses provided by XFELs has enabled direct, unambiguous imaging of coherent acoustic phonons in gold nanocrystals in three dimensions. The technique demonstrated here can

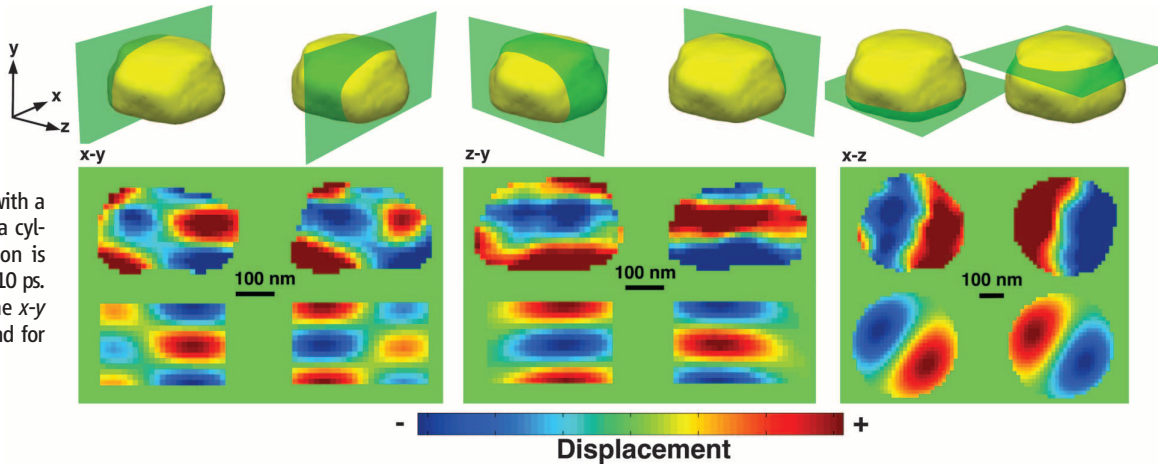

Fig. 4. Comparison of data with theory. Orthogonal slices taken either side of the center (**top**) of nanocrystal I compare the projected displacement obtained from the experiment (**middle**) with a simulated (1, 1) mode for a cylinder (**bottom**). Comparison is made for a delay time of +110 ps. The separation between the *x-y* and *y-z* slices is 180 nm and for the *x-z* slices 120 nm.

be applied widely to investigate other materials such as semiconductors and nanostructures and, with continued improvement in experimental design, it should be possible to image particles with sizes less than 100 nm. Many other applications will become possible with the advent of coherent, ultrashort electron sources (*28*), which could provide atomic-scale images when used with diffractive imaging.

References and Notes

1. C. Rose-Petruck *et al.*, *Nature* **398**, 310–312 (1999).
2. C. W. Siders *et al.*, *Science* **286**, 1340–1342 (1999).
3. B. J. Siwick, J. R. Dwyer, R. E. Jordan, R. J. D. Miller, *Science* **302**, 1382–1385 (2003).
4. K. Sokolowski-Tinten *et al.*, *Nature* **422**, 287–289 (2003).
5. J. Chen, W.-K. Chen, J. Tang, P. M. Rentzepis, *Proc. Natl. Acad. Sci. U.S.A.* **108**, 18887–18892 (2011).
6. A. M. Lindenberg *et al.*, *Phys. Rev. Lett.* **84**, 111–114 (2000).
7. D. M. Fritz *et al.*, *Science* **315**, 633–636 (2007).
8. R. Ernstorfer *et al.*, *Science* **323**, 1033–1037 (2009).
9. A. Cavalleri *et al.*, *Nature* **442**, 664–666 (2006).
10. M. Turner *et al.*, *Nature* **454**, 981–983 (2008).
11. S. A. Maier *et al.*, *Adv. Mater.* **13**, 1501–1505 (2001).
12. M. S. Hanay *et al.*, *Nat. Nanotechnol.* **7**, 602–608 (2012).
13. G. V. Hartland, *J. Chem. Phys.* **116**, 8048 (2002).
14. M. Pelton *et al.*, *Nat. Nanotechnol.* **4**, 492–495 (2009).
15. M. A. van Dijk, M. Lippitz, M. Orrit, *Phys. Rev. Lett.* **95**, 267406 (2005).
16. C.-Y. Ruan, Y. Murooka, R. K. Raman, R. A. Murdick, *Nano Lett.* **7**, 1290–1296 (2007).
17. A. Plech, V. Kotaidis, S. Grésillon, C. Dahmen, G. von Plessen, *Phys. Rev. B* **70**, 195423 (2004).
18. P. Emma *et al.*, *Nat. Photonics* **4**, 641–647 (2010).
19. J. Miao, P. Charalambous, J. Kirz, D. Sayre, *Nature* **400**, 342–344 (1999).
20. M. A. Pfeifer, G. J. Williams, I. A. Vartanyants, R. Harder, I. K. Robinson, *Nature* **442**, 63–66 (2006).
21. Materials and methods are available as supplementary materials on *Science* Online.
22. M. C. Newton, S. J. Leake, R. Harder, I. K. Robinson, *Nat. Mater.* **9**, 120–124 (2010).
23. P. Hart *et al.*, *Proc. SPIE* **8504**, 85040C (2012).
24. P. B. Allen, *Phys. Rev. Lett.* **59**, 1460–1463 (1987).
25. G. V. Hartland, M. Hu, J. E. Sader, *J. Phys. Chem. B* **107**, 7472–7478 (2003).
26. K. Ichiyanagi *et al.*, *Phys. Rev. B* **84**, 024110 (2011).
27. J. R. Fienup, *Appl. Opt.* **21**, 2758–2769 (1982).
28. A. J. McCulloch *et al.*, *Nat. Phys.* **7**, 785–788 (2011).

Acknowledgments: This work was supported by FP7 advanced grant from the European Research Council. I.K.R is appreciative of support from the Engineering and Physical Sciences Research Council (EPSRC) under grant EP/I022562/1 and from the Biotechnology and Biological Sciences Research Council (BBSRC) under grant BB/H022597/1. A.H. was supported by Atomic Weapons Establishment. J.S.W. is grateful for support from the UK EPSRC under grant EP/H035877/1. A.M.K. is grateful for support from the EPSRC under grant EP/I020691/1. B.A. acknowledges the support of the Australian Research Council Centre of Excellence for Coherent X-ray Science. The experimental work was carried out at the Linac Coherent Light Source, a National User Facility operated by Stanford University on behalf of the U.S. Department of Energy, Office of Basic Energy Sciences. We acknowledge S. Boutet for insightful discussion.

Supplementary Materials

www.sciencemag.org/cgi/content/full/science.1236034/DC1
Materials and Methods
Figs. S1 and S2
Table S1
References (*29*–*40*)
Movie S1

4 February 2013; accepted 7 May 2013
Published online 23 May 2013;
10.1126/science.1236034

Chiral Symmetry Breaking in Superfluid ^{3}He-A

H. Ikegami,[1,2]* Y. Tsutsumi,[3] K. Kono[1,2]

Spontaneous symmetry breaking is an important concept in many branches of physics. In helium-3 (^{3}He), the breaking of symmetry leads to the orbital chirality in the superfluid phase known as ^{3}He-A. Chirality is a fundamental property of ^{3}He-A, but its direct detection has been challenging. We report direct detection of chirality by transport measurements of electrons trapped below a free surface of ^{3}He-A. In particular, we observed the so-called intrinsic Magnus force experienced by a moving electron; the direction of the force directly reflected the chirality. We further showed that, at the superfluid transition, the system selected either right- or left-handed chirality. The observation of such selection directly demonstrates chiral symmetry breaking.

Spontaneous symmetry breaking plays an essential role in phase transitions. It occurs in systems that have multiple ground states of equal energy. Symmetry is broken when the system settles into a particular ground state. This process can result in marked changes to the properties of the system. One notable consequence of symmetry breaking is the orbital chirality in the A phase of the superfluid ^{3}He (^{3}He-A), which emerges from the symmetric normal ^{3}He (*1*, *2*). In ^{3}He-A, ^{3}He atoms form Cooper pairs of orbital angular momentum $L = 1$, and the angular momenta of all the pairs are oriented in the same direction denoted by the unit vector $\hat{l}$. The chirality is characterized by the orientation of $\hat{l}$, and its meaning becomes clear by considering the orbital motion just near a surface: Because of the boundary condition ($\hat{l} \| \hat{z}$, where $\hat{z}$ is the surface normal) (*3*), all the Cooper pairs rotate in either a right- or left-handed direction around $\hat{z}$ ($\hat{l} = +\hat{z}$ or $\hat{l} = -\hat{z}$, respectively). These two chiral states are a degenerate time-reversal pair, and the selection of either state amounts to spontaneous chiral symmetry breaking (*4*). Chirality was detected only

[1]Low Temperature Physics Laboratory, RIKEN, Wako, Saitama 351-0198, Japan. [2]The RIKEN Center for Emergent Matter Science, RIKEN, Wako, Saitama 351-0198, Japan. [3]Condensed Matter Theory Laboratory, RIKEN, Wako, Saitama 351-0198, Japan.

*Corresponding author. E-mail: hikegami@riken.jp